remote sensing

MDPI

Article

Assessment of MODIS and VIIRS Ice Surface Temperature Products over the Antarctic Ice Sheet

Chenlie Shi [1,2], Ninglian Wang [1,2,3,*], Yuwei Wu [1,2], Quan Zhang [1,2], Carleen H. Reijmer [4] and Paul C. J. P. Smeets [4]

[1] Shaanxi Key Laboratory of Earth Surface System and Environmental Carrying Capacity, College of Urban and Environmental Sciences, Northwest University, Xi'an 710127, China; max1995@stumail.nwu.edu.cn (C.S.)
[2] Institute of Earth Surface System and Hazards, College of Urban and Environmental Sciences, Northwest University, Xi'an 710127, China
[3] Institute of Tibetan Plateau Research, Chinese Academy of Sciences, Beijing 100101, China
[4] Institute for Marine and Atmospheric Research Utrecht, Utrecht University, 3584 CS Utrecht, The Netherlands
* Correspondence: nlwang@nwu.edu.cn

Abstract: The ice surface temperature (IST) derived from thermal infrared remote sensing is crucial for accurately monitoring ice or snow surface temperatures in the polar region. Generally, the remote sensing IST needs to be validated by the in situ IST to ensure its accuracy. However, due to the limited availability of in situ IST measurements, previous studies in the validation of remote sensing ISTs are scarce in the Antarctic ice sheet. This study utilizes ISTs from eight broadband radiation stations to assess the accuracy of the latest-released Moderate Resolution Imaging Spectroradiometer (MODIS) IST and Visible Infrared Imager Radiometer Suite (VIIRS) IST products, which were derived from two different algorithms, the Split-Window (SW-based) algorithm and the Temperature–Emissivity Separation (TES-based) algorithm, respectively. This study also explores the sources of uncertainty in the validation process. The results reveal prominent errors when directly validating remote sensing ISTs with the in situ ISTs, which can be attributed to incorrect cloud detection due to the similar spectral characteristics of cloud and snow. Hence, cloud pixels are misclassified as clear pixels in the satellite cloud mask during IST validation, which emphasizes the severe cloud contamination of remote sensing IST products. By using a cloud index (n) to remove the cloud contamination pixels in the remote sensing IST products, the overall uncertainties for the four products are about 2 to 3 K, with the maximum uncertainty (RMSE) reduced by 3.51 K and the bias decreased by 1.26 K. Furthermore, a progressive cold bias in the validation process was observed with decreasing temperature, likely due to atmospheric radiation between the radiometer and the snow surface being neglected in previous studies. Lastly, this study found that the cloud mask errors of satellites are more pronounced during the winter compared to that in summer, highlighting the need for caution when directly using remote sensing IST products, particularly during the polar night.

Keywords: Antarctic ice sheet; MODIS; VIIRS; ice surface temperature; validation; broadband radiation

Academic Editor: Yi Luo

Received: 11 February 2025
Revised: 28 February 2025
Accepted: 5 March 2025
Published: 7 March 2025

Citation: Shi, C.; Wang, N.; Wu, Y.; Zhang, Q.; Reijmer, C.H.; Smeets, P.C.J.P. Assessment of MODIS and VIIRS Ice Surface Temperature Products over the Antarctic Ice Sheet. *Remote Sens.* **2025**, *17*, 955. https://doi.org/10.3390/rs17060955

1. Introduction

The ice/snow surface temperature (IST) typically refers to the temperature measured a few micrometers above the interface where the snow surface contacts the atmosphere [1,2]. The IST plays a crucial role in governing the process of energy and water exchange between the snow surface and the atmosphere [3] and directly affects snow surface melt, mass balance, and atmospheric circulation patterns [4,5]. The polar regions, as the largest reservoirs of ice on Earth, are particularly sensitive to global climate change [6]. Previous studies have shown that the warming of the Arctic is two to three times [7], or even four times [8], that of global warming, mainly due to the "Arctic Amplification" effect. In contrast, the Antarctic is a continent covered by ice and snow, surrounded by ocean, and its temperature changes over the past few decades have been complex, with prominent spatial differences due to using different data sources [9,10].

The monitoring of IST variations over the Antarctic ice sheet mainly includes the following three data sources: automatic weather station (AWS) data [11,12], thermal infrared remote sensing observation data [13,14], and climate model or reanalysis data [10,15]. The AWS temperature has played a crucial role in monitoring climate change in the Antarctic over the past few decades [16]. However, due to extreme and complex weather events that often occur over the Antarctic ice sheet, coupled with katabatic winds [17], AWSs are usually sparsely deployed and mostly concentrated in the coastal areas, which cannot be representative of temperature changes for the entire Antarctic ice sheet. Furthermore, most AWSs are not equipped with broadband radiometers, where they usually use temperature and humidity instruments to measure the 2 m air temperature [16] rather than the IST. Meanwhile, climate model or reanalysis outputs also introduce uncertainties in IST estimation, primarily due to the limited measured data availability and a poor understanding of key processes over the snow surface [4]. In addition, reanalysis products typically exhibit substantial warm biases in the polar region [18], which are more pronounced in areas with a strong temperature inversion, such as the interior of the Antarctic plateau [19]. Consequently, the remote sensing IST becomes the preferred data source for accurately observing the IST over the entire continent of the Antarctic [20,21].

Thermal infrared sensors, such as the Advanced Very High Resolution Radiometer (AVHRR) [22], Moderate Resolution Imaging Spectroradiometer (MODIS) [23], and Visible Infrared Imager Radiometer Suite (VIIRS) [24], which can be used to retrieve ISTs, have been widely applied for monitoring temperature changes and ice surface melt in the Arctic in the past [14,25–27] due to their twice-daily revisit cycles (more frequent in the polar region) and relatively high spatial resolution. The AVHRR IST data were used to study spatiotemporal variation in temperature over the entire Antarctic from 1982 to 1998 [13]. Subsequently, more studies utilized the AVHRR IST to study temperature changes and their relationship with ice surface melt and albedo in the Arctic and Greenland [28,29]. However, the limited spectral bands of the AVHRR sensor, combined with the similar spectral properties of clouds, ice, and snow, result in challenges with cloud mask products in the polar region [30], which may further lead to potential issues in trend analyses. Since the MODIS sensor carried on the terra satellite was launched in 1999 [31], it has become an important and widely used sensor in tracking global changes in the surface that have more than twenty bands, and the VIIRS sensor will inherit the MODIS sensor to generate continuous climate data within a few years [32]. However, the remote sensing ISTs derived from the MODIS and VIIRS sensors require extensive validation for different areas and climate regions before their application to ensure temperature data reliability and improve the accuracy of retrieval algorithms. Although progress has been made in validating MODIS and VIIRS surface temperatures, it is mainly concentrated in the middle and low latitudes [33–35], as well as in the Arctic [36,37] and Greenland [3,38] for the cryosphere. Table 1 provides the summary statistics for the IST validation results in the polar region from previous studies. From Table 1, it can be seen that the validation work conducted in the Antarctic using radiation data is still limited, primarily due to the very few directly available stations in the region [4]; further validation efforts are needed to ensure the accuracy and reliability of IST data derived from the MODIS sensor in the Antarctic region, and especially for the VIIRS sensor, which has not been evaluated in the Antarctic ice sheet before.

Table 1. Summary statistics for the IST validation results in the polar region from previous studies (T_a, T_{nar}, and T_{bro} are the near-surface air temperature, narrowband radiation IST, and broadband radiation IST, respectively).

Year	Study Area	In Situ Data	Satellite Product	Product Level	Bias	RMSE	References
2004	Arctic sea ice South pole	T_a	MOD29	swath	ALL: −2.1° Cloud filter: −0.9° Cloud filter: −1.2°	ALL: −3.7° Cloud filter: −1.6° Cloud filter: 1.7°	[39]
2008	Greenland	T_a	MOD11 Landsat ASTER	swath	−0.3°	−2.1°	[5]
2011	Svalbard	T_{nar}	MOD11	swath		All: −1.5~−6° Average: −3°	[40]
2012	Arctic sea ice	T_a T_{nar}	AVHRR Sea ice	swath	−3.43° −1.81°	4.29° 1.02°	[41]
2012	Barrow, Alaska	T_a	MOD11	daily	−1.8°	4°	[42]
2013	Antarctica	T_a	MOD11	month	−8.08~−2.87°		[21]
2014	Svalbard	T_{bro}	MOD11	daily	ALL: −3.3° Cloud filter: −0.3°	ALL: 5.3° Cloud filter: 3°	[43]
2014	Antarctica	T_{bro}	MOD11	daily	−1.8~0°	2.2~4.8°	[4]
2014	Summit, Greenland	T_a	MOD29	swath	−5~−0.5°		[38]
2018	Summit, Greenland	T_a T_{nar}	MOD11	swath	−1.9° ALL: −0.7° Cloud filter: −0.4	3.1° ALL: 1.6° Cloud filter: 1°	[2]
2020	Arctic sea ice	T_a	Landsat	swath	−3.74~−0.98°	2.17~5.15°	[44]
2023	Greenland	T_a T_{bro}	MOD11	swath	−4.5° Cloud filter: −2.4°	5.2° Cloud filter: 3.2°	[45]

In the Antarctic, the water vapor content is quite low, and the IST can reach minus eighty degrees inland [46]. Due to the bad weather and special environment, the validation and the source of uncertainty in remote sensing IST are still not fully understood. Firstly, some studies tried to validate the remote sensing IST products using air temperature over the Antarctic ice sheet [21,46,47]. However, obvious differences exist between the air temperature and the IST, especially in the polar region where the near-surface temperature inversion is common [2]. Generally, in situ ISTs derived from narrow infrared radiation and broadband radiation are recommended to validate remote sensing ISTs [48,49]. Secondly, the sparse and uneven distribution of radiation stations in the Antarctic pose challenges for the remote sensing IST validation, with only a handful of validations having been made using the radiation data [4,50]. Thirdly, most of the validation work is focused on the Split-Window algorithm (SW-based) IST product for the polar region [3,5,21], but the remote sensing IST products based on the Temperature–Emissivity Separation (TES-based) method have not yet been validated in the polar region.

For the above reasons, this study utilized the in situ ISTs from eight broadband radiation stations to evaluate the latest released MODIS and VIIRS IST products in the Antarctic ice sheet, which were retrieved from the SW-based algorithm and the TES-based algorithm, respectively. A cloud index (n) was used to evaluate the impact of incorrect cloud identification of satellite sensors on IST validation and the seasonal variations in validation results. Finally, the reasons that may affect the validation accuracy were discussed.

2. Data and Method

2.1. Study Area and Station Data

2.1.1. Study Area

The Antarctic ice sheet is situated at the southernmost point of the Earth, is encircled entirely by oceans, and is divided into three distinct regions, including the Antarctic peninsula, the west Antarctic, and the east Antarctic (see Figure 1). Covering an area of 14.2 million square kilometers [51], the Antarctic ice sheet stands out as the coldest, driest, and highest continent, with an average elevation of 2500 m. The unique geographical and topographical features contribute to its harsh climate, making it more extreme than any other region on Earth.

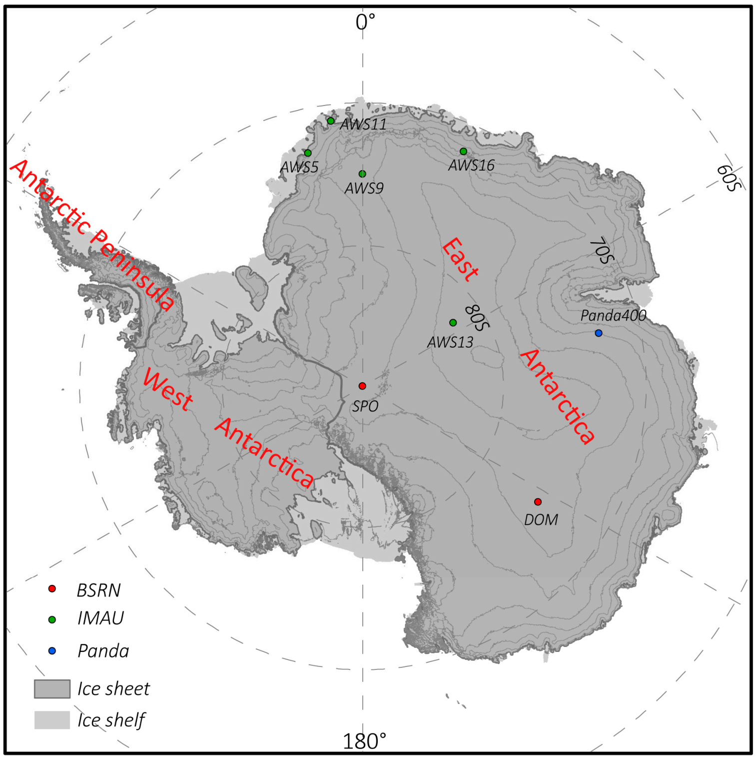

Figure 1. The spatial distribution of the Antarctic ice sheet and eight broadband radiation stations. The stations with red color belong to the BSRN, green for the IMAU, and blue for Panda.

2.1.2. Station Data

Due to the limited availability of publicly accessible narrow infrared radiation data in the Antarctic, this study relies exclusively on the IST derived from broadband radiation data to evaluate the accuracy of the remote sensing IST. Although previous studies have demonstrated that the IST derived from broadband radiation is less accurate than that based on narrow infrared radiation data [52,53], it has also been widely used for surface temperature validation in mid- and low-latitude regions [48], as well as in high-latitude snow surfaces [40,43] or the Greenland ice sheet [3,45]. In this study, eight broadband radiation stations representing diverse regions of the Antarctic, including the inland plateau, the katabatic wind zones, and the coastal areas, were selected. The specific locations of these stations are illustrated in Figure 1. These stations are primarily managed by three agencies: the Institute for Marine and Atmospheric Research at Utrecht University (IMAU), the Baseline Surface Radiation Network (BSRN), and the Panda AWS network (Panda). The IMAU AWS provides broadband radiation data alongside meteorological observations such as air temperature, wind speed and direction, air pressure, and relative humidity [54]. In this study, AWS5, AWS9, AWS11, AWS13, and AWS16 were selected for the remote sensing IST validation. The data can be obtained by corresponding to C.J.P.P. Smeets. The BSRN data, available at https://bsrn.awi.de/, include the DOM (only broadband radiation data) and SPO sites (both radiation and meteorological data) in this study [55]. Similarly, the Panda AWS network, operated by the Chinese National Antarctic Research Expedition (CHINARE), collects the basic meteorological and radiation data along the PANDA transect; only the Panda400 station with broadband radiation data were selected [56]. Detailed descriptions of these station data for this study are shown in Table 2.

Table 2. Detailed descriptions of the eight stations. T_{2m} (RH_{2m}) is the air temperature (relative humidity) of 2 m.

Agency	Station Name	Longitude	Latitude	Elevation (m)	Downward Broadband Radiation	Upward Broadband radiation	T_{2m}	RH_{2m}	Temporal Resolution	Time Range
IMAU	AWS5	−73.10	−13.17	360	yes	yes	yes	yes	60 min	1 January 2013–31 December 2013
	AWS9	−75.00	0.00	2900	yes	yes	yes	no	60 min	1 January 2018–31 December 2018
	AWS11	−71.17	−6.80	690	yes	yes	yes	no	60 min	1 January 2016–31 December 2016
	AWS13	−82.12	55.03	3730	yes	yes	yes	yes	60 min	1 January 2015–31 December 2015
	AWS16	−71.95	23.33	1300	yes	yes	yes	yes	60 min	1 July 2019–30 June 2020
PANDA	Panda400	−72.86	77.38	2572	yes	yes	yes	yes	60 min	1 January 2020–31 December 2020
BSRN	DOM	−75.10	123.38	3233	yes	yes	no	no	1 min	1 January 2018–31 December 2018
	SPO	−89.98	−24.80	2800	yes	yes	yes	yes	1 min	1 January 2015–31 December 2015

Generally, the uncertainty of the air temperature obtained from an AWS is less than 0.3°, and the uncertainty of relative humidity (RH) is approximately 2% for a RH < 90% and 3% for a RH > 90% [57]. For the broadband radiometers, the maximum daily uncertainty during laboratory calibration is reported to be about 10% [56,57]. However, under actual comparison outdoors, the uncertainty of a broadband radiometer is typically lower than 10%, which is discussed in detail in Section 4.1. Furthermore, the harsh environment in the Antarctic ice sheet poses severe challenges for the long-term station observations, resulting in the limited availability of continuous data. Therefore, the station data covering a complete year was selected for the IST validation.

2.1.3. Preprocessing of Station Data

To evaluate the accuracy of the remote sensing IST, in situ ISTs sampled at 60 min intervals were resampled to 10 min intervals, which minimizes the impact of temporal discrepancies between the satellite overpass time and the station observation time. In practice, the IST varies very little within an hour due to the high solar zenith angle and the high albedo of snow in the polar region. Additionally, the eight stations are situated on a homogeneous snow surface, ensuring minimal impact due to spatial heterogeneity, which has been demonstrated in previous studies [45]. The in situ IST was calculated using Stefan–Boltzmann's law based on the upward and downward broadband radiation measurements and the broadband emissivity of snow surface. The specific formula is as follows:

$$IST_s = \left[\frac{LW_{up} - (1-\varepsilon)LW_{down}}{\varepsilon\sigma}\right]^{\frac{1}{4}} \quad (1)$$

where IST_s is the in situ IST value, LW_{up} and LW_{down} are the upward broadband radiation and the downward broadband radiation, respectively, σ is the Stefan–Boltzmann constant (5.67×10^{-8} w/m^2/k^4), and ε is the broadband emissivity of snow set as 0.985 according to previous studies [3,40].

Meanwhile, the anomalous values in the station also need to be excluded due to the harsh environment over the Antarctic ice sheet. The specific steps are as follows: (1) the obvious outliers in the upward radiation and the downward broadband radiation measurements were identified and eliminated using the three-sigma method [58]; (2) the values with an extremely large difference between the air temperature and in situ IST were removed by manual screening, which may be due to the anomalies in the air temperature or the IST; (3) the LW_{down} values typically cannot exceed the LW_{up}, and the corresponding radiation values were excluded if the LW_{down} values were greater than the LW_{up} [59]; (4) for the stations at the inland plateau, rime or ice is often present. Therefore, the data records with an RH greater than 97% (corresponding to a 3% uncertainty) were excluded [17]. By implementing these steps, the anomalous values in the station were effectively removed, minimizing the impact of random errors on the IST validation results.

2.2. MODIS and VIIRS IST Products

The ISTs derived from the MODIS sensor onboard the Aqua satellite and the VIIRS sensor onboard the Suomi-NPP satellite were used for the evaluation in this study; both satellites overpass during the local afternoon. For clarity, the MODIS (VIIRS) IST products derived from the SW-based algorithm are designated as MYD11 (VNP11), while the products based on the TES-based algorithm are referred to as MYD21 (VNP21). The four products analyzed in this study were generated using the latest algorithms (version 6.1) and were provided as level 2 swath products. Detailed descriptions of the SW-based algorithm and the TES-based algorithm are as follows:

2.2.1. SW-Based Algorithm

The theory of the SW-based algorithm utilizes a linear or nonlinear fitting relationship to correct for the atmospheric influences based on the disparity in water vapor absorption between the 11 μm and the 12 μm channels [1]. The SW-based algorithm is the simplest and most effective IST retrieval method, which has been widely used to retrieve IST data in the past.

The MYD11 product is derived from the General Split Window algorithm (GSW) [60]. The specific expression is as follows:

$$\begin{aligned} IST_m = b_0 &+ \left(b_1 + b_2\frac{1-\varepsilon}{c} + b_3\frac{\Delta\varepsilon}{\varepsilon^2}\right)\frac{T_{31}+T_{32}}{2} \\ &+ \left(b_4 + b_5\frac{1-\varepsilon}{\varepsilon} + b_6\frac{\Delta\varepsilon}{\varepsilon^2}\right)\frac{T_{31}-T_{32}}{2} + b_7(T_{31}-T_{32})^2 \end{aligned} \quad (2)$$

where IST_m is the MODIS IST value; T_{31} and the T_{32} are the brightness temperatures of MODIS band 31 and band 32, respectively; $\Delta\varepsilon = \varepsilon31 - \varepsilon32$ and $\varepsilon = \frac{\varepsilon31 + \varepsilon32}{2}$, where $\varepsilon31$ and $\varepsilon32$ are the snow emissivity values corresponding to MODIS band 31 and band 32, respectively; and b_n (n from 0 to 6) is the coefficients of the GSW algorithm. Refer to [60] for details about the GSW algorithm.

The enterprise algorithm is used to retrieve the VIIRS IST (VNP11), which has replaced the previous SW-based method for the VIIRS sensor [61]. The new enterprise algorithm is simple, robust, and flexible, aiming to produce consistent IST products [33], and the VNP11 product can be gained beginning with July 2019. Considering the availability of station data, only two stations are used to validate the accuracy of the VNP11 product in this study. The expression of the enterprise algorithm is as follows:

$$IST_v = C + A_1 T_{15} + A_2 (T_{15} - T_{16}) + A_3 \varepsilon + A_4 \varepsilon \, (T_{15} - T_{16}) + A_5 \Delta\varepsilon \tag{3}$$

where IST_v is the VIIRS IST value; T_{15} and T_{16} are the brightness temperatures of VIIRS band 15 and band 16, respectively; and $\Delta\varepsilon = \varepsilon 15 - \varepsilon 16$ and $\varepsilon = \frac{\varepsilon 15 + \varepsilon 16}{2}$, where $\varepsilon 15$ and $\varepsilon 16$ are the emissivity values corresponding to VIIRS band 15 and band 16, respectively. C, A_1, A_2, A_3, A_4, and A_5 are the VNP11 algorithm coefficients. For the detailed theoretical analysis and calculation process, refer to [33].

2.2.2. TES-Based Algorithm

The MYD21 and the VNP21 products, derived from the TES-based algorithm, are designed to create a long-term, consistent climate data record to address the discrepancies of SW-based algorithms between the MODIS and VIIRS [62]. The TES-based algorithm usually requires at least three thermal infrared bands within the 8–12 µm range, with at least one band located in the 8–9 µm atmospheric window. For the official surface temperature products, the MERRA-2 reanalysis product was used to perform the atmosphere correction and to obtain the surface radiation [62], where the accuracy of atmospheric reanalysis data directly affects the accuracy of surface outgoing radiation. Once the surface radiation is determined, the TES-based algorithm is dynamically employed to retrieve the IST and ice surface emissivity (ISE). This method comprises three primary modules: the NEM module, the Ratio module, and the MMD module. For a detailed algorithm introduction, please refer to [62,63].

2.2.3. Preprocessing of MODIS and VIIRS IST Products

A Quality Control (QC) layer in the remote sensing IST products was performed to exclude the outlier values, where bit 0–1 with a value of '00' was flagged as a "good pixel", and no further screening was performed. Consequently, only the pixel labeled as a "good pixel" or "clear sky" was selected for subsequent IST validation. It is worth noting that bit 0–1 for the VNP11 only acquires values of a zenith angle less than 40 degrees, and bit 2–3 equal to '00' can extract the values for whole sensor zenith angle (corresponding with Yuling Liu, the author of the VNP11 product). But the vacant IST values caused by the bow-tie effect of VIIRS images are filled in the level 2 swath product, which leads to a serious cold bias in the polar region due to the incorrect cloud mask and other reasons. Hence, the VNP11 data with the zenith angle greater than 40 degrees were excluded in this study.

2.3. A Cloud Index

A cloud index (n) was used to identify whether the sky is clear or cloudy from the station perspective, which was calculated based on the relationship between the air temperature and the downward broadband radiation. Generally, the atmospheric downward broadband radiation for a given temperature under a clear sky condition is lower than the broadband radiation under the cloudy condition at the same temperature [57,64]. Theoretically, the maximum atmosphere downward broadband radiation can be regarded as blackbody radiation under a given air temperature. In this scenario, the radiative exchange between the atmosphere and the surface reaches a thermal equilibrium. To define the boundaries for the cloud index, the lowest 5th percentile of the broadband radiation corresponds to a given temperature value to perform a quadratic polynomial fit as the lower boundary, and the upper bound is the blackbody radiation value at a given air temperature. The 5th percentile value is selected to minimize the fitting errors caused by outliers. These two fitting lines for the lower boundary and the upper boundary correspond to a cloud index of 0 and 1, where 0 represents no cloud and 1 represents completely cloudy. Assuming the cloud amount increases linearly at a given temperature, a different downward broadband radiation at a given air temperature can yield a cloud index (n) between 0 and 1, where n closer to 0 indicates a clear sky and closer to 1 indicates a cloudy sky. Based on previous studies and actual conditions [43], this study considers a value of the cloud index less than 0.2 to be a clear sky condition, values between 0.2 and 0.8 to be mixed conditions, and values greater than 0.8 to be completely cloudy. As mentioned earlier in this article, due to the unavailability of air temperature data at the DOM station, the cloud index at the DOM cannot be obtained.

2.4. Assessment Method

A two-step validation was performed to evaluate the accuracy of the MODIS and VIIRS IST products. In the first step, the in situ IST values are compared with the remote sensing IST identified as clear-sky pixels based on the satellite cloud mask product, and the assessment accuracies can be found in Section 3.1. Based on the first step, by using the cloud index to further eliminate the pixels classified as clear sky in the satellite cloud mask but cloud-covered pixels, remaining matching sequences values were evaluated again in the second step, and the validation results are shown in Section 3.2. Therefore, Section 3.1 presents the preliminary assessment results of the remote sensing IST products, while Section 3.2 is the validation accuracy of the IST retrieval algorithm, and the assessment differences between Sections 3.1 and 3.2 represent the impact of misidentifying cloudy pixels in the remote sensing IST validation. Three statistical metrics, including the correction coefficient (CC), bias, and root mean square (RMSE) were chosen to evaluate the accuracies of the MODIS and VIIRS IST products. The specific formulas are as follows:

$$Bias = \frac{\sum_{i=1}^{N}(IST_{rs} - IST_s)}{N} \tag{4}$$

$$RMSE = \sqrt{\frac{\sum_{i=1}^{N}(IST_{rs} - IST_s)^2}{N}} \tag{5}$$

$$CC = \frac{\sum_{i=1}^{N}\left(IST_{rs} - \overline{IST}_{rs}\right)\left(IST_s - \overline{IST}_s\right)}{\sqrt{\sum_{i=1}^{N}\left(IST_{rs} - \overline{IST}_{rs}\right)^2}\sqrt{\sum_{i=1}^{N}\left(IST_s - \overline{IST}_s\right)^2}} \tag{6}$$

where N is the number of IST pixels, IST_{rs} is the remote sensing IST value, and IST_s is the corresponding in situ IST data.

3. Results

3.1. Preliminary Assessment Results of MODIS and VIIRS Products

The QC layer of the satellite products was used to obtain theoretical clear sky IST values for validation. Figures 2 and 3 are the validation results of the MYD11 and MYD21 products, respectively, where the assessment accuracy is for a whole year. For the MYD11 product, the CC is between 0.95 and 0.99, indicating a very strong correlation between in situ IST data and the remote sensing IST. The biases vary from −1.29 K to −3.83 K, where the biases for AWS9 and AWS16 are greater than −3 K. The RMSEs for the eight stations vary from 2.23 K to 5.13 K, and only the RMSE of AWS9 is greater than 5 K. There are prominent validation discrepancies between the different stations, particularly for AWS9, which has a larger bias and RMSE. This may be attributed to the data affected by rime that were not excluded using the RH as a filtering criterion (see Table 2). Additionally, the differences in cloud occurrence frequency and the accuracy of MODIS cloud detection across stations also contribute to the validation discrepancies observed between the different stations, as referenced in Section 4.2. For the MYD21, the biases are from −0.59 K to −2.53 K and the RMSEs are 1.93 K to 3.88 K for seven stations (excluding the SPO station). Notably, there is an obvious warm bias for the SPO site, which may be related to the incorrect atmosphere correction for the TES-based algorithm over the Antarctic plateau. In the Antarctic inland region, particularly during winter, the reanalysis temperature data often exhibits a certain warm bias [4,19]. Consequently, incorporating warm atmospheric conditions into the atmospheric correction prior to the TES-based algorithm retrieval may result in the warm bias of the IST validation. Further details on the uncertainties of atmospheric correction in the TES-based algorithm, please refer to [65].

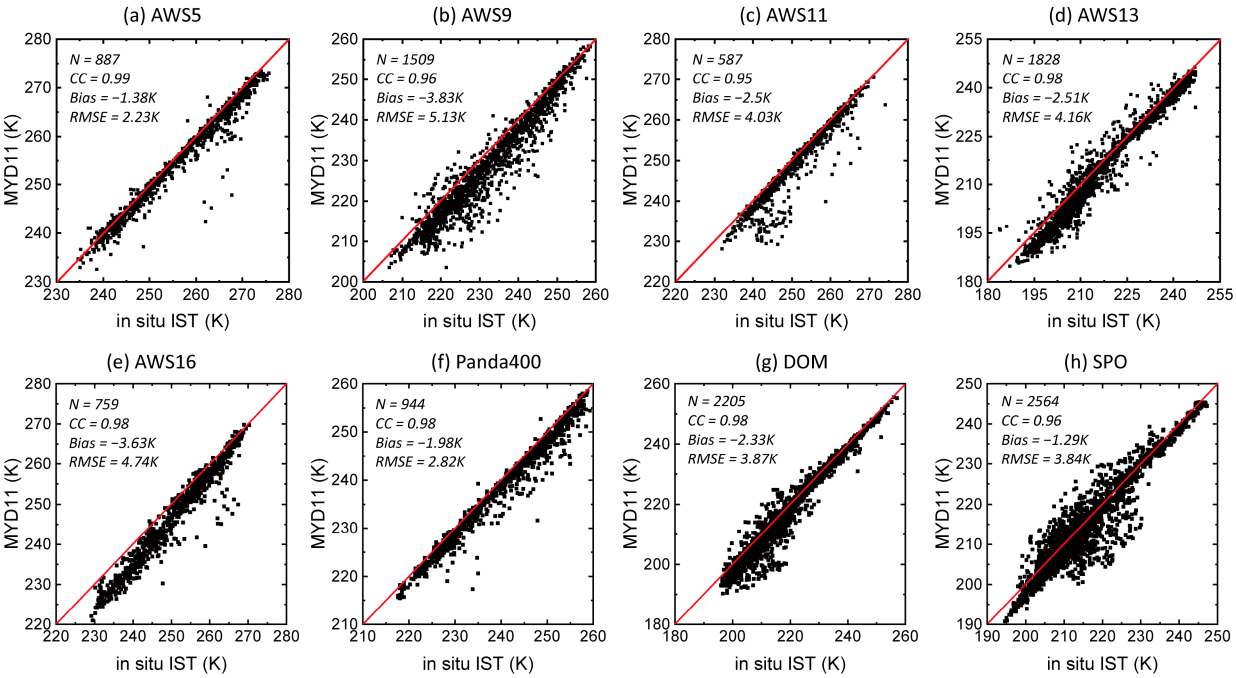

Figure 2. Scatterplots of comparison results between MYD11 products and in situ IST for eight stations.

Figures 4 and 5 are the assessment results for the VNP21 and VNP11 products. For the VNP21, the CC for SPO is 0.85, and the CC for other stations varies from 0.91 to 0.99. The biases are between −0.96 K and −2.21 K (excluding AWS13, DOM, and SPO). The RMSEs vary from 1.82 K to 3.87 K (excluding SPO for 5.48 K). AWS13, DOM, and SPO have a certain warm bias (0.83 K, 0.82 K, and 3.84 K); the scatterplots in Figure 4 reveal that the warm bias mainly occurs during winter, and these stations are in the interior of the Antarctic plateau. As with the MYD21, the warm bias is likely attributed to the uncertainties in atmospheric reanalysis data over the Antarctic interior during winter, which adversely affect the atmospheric corrections before performing the TES-based algorithm. For the VNP11, the CC is between 0.97 and 0.99, biases vary from −1.06 K to 0.26 K, and RMSEs are from 1.51 K to 2.03 K.

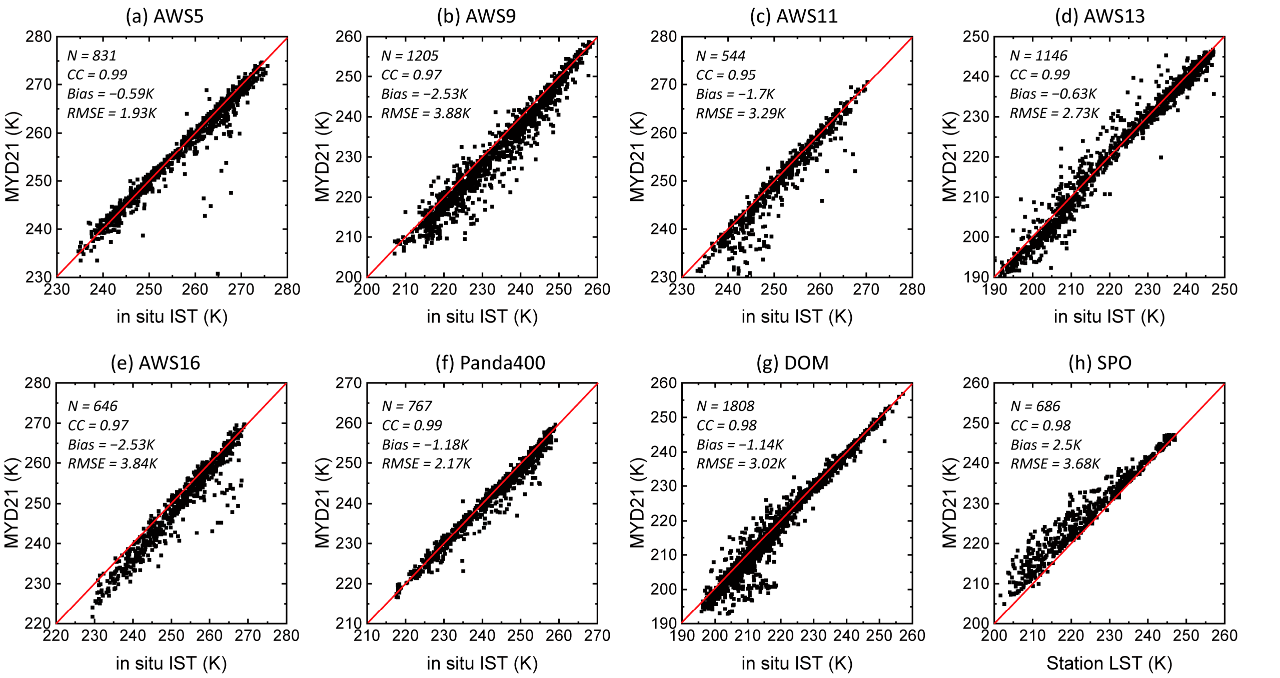

Figure 3. Scatterplots of comparison results between MYD21 products and in situ IST for eight stations.

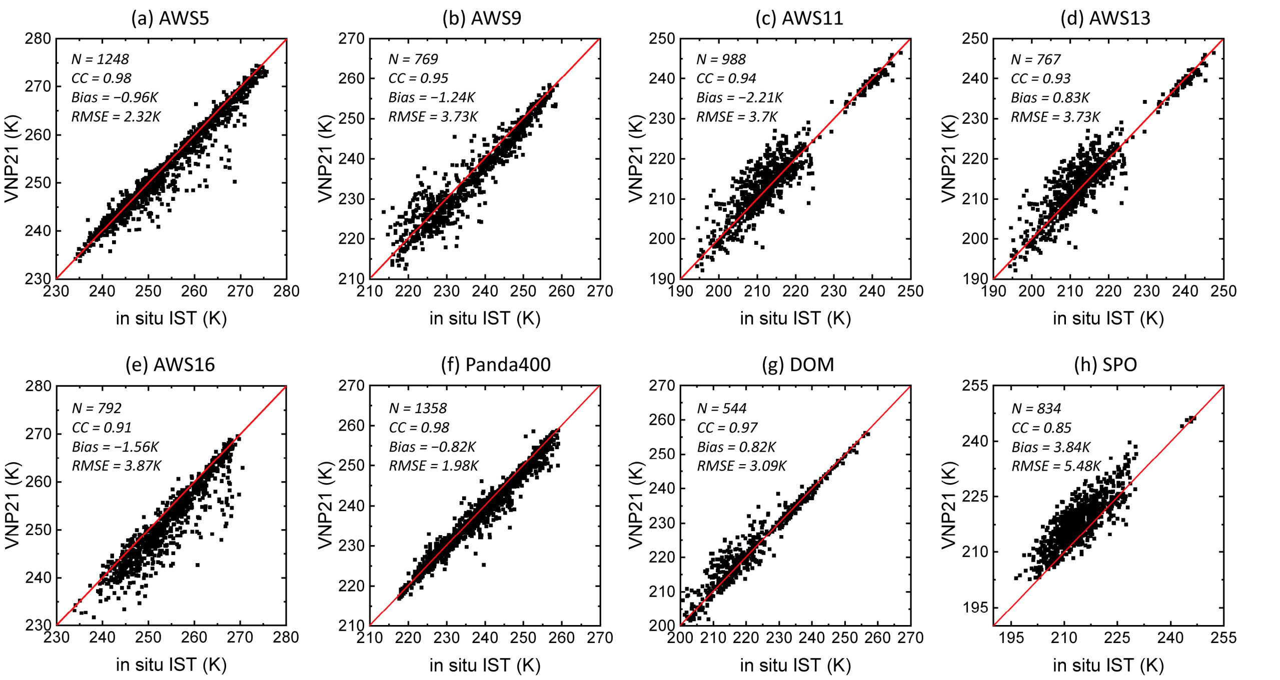

Figure 4. Scatterplots of comparison results between VNP21 products and in situ IST for eight stations.

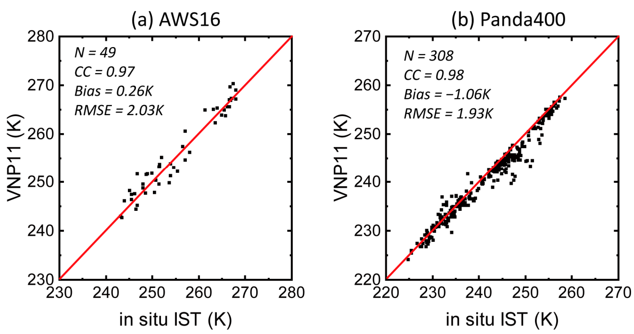

Figure 5. Scatterplots of comparison results between VNP11 products and in situ IST for two stations.

To analyze the seasonal differences in the IST validation results, Table 3 exhibits the assessment accuracies of the four IST products in summer (DJF) and winter (JJA). In Table 3, the biases and RMSEs for most stations in summer are lower compared to the validation results in winter. Additionally, there is a larger cold bias relative to winter in AWS5, which can be attributed to the fact that the pixels with clouds are counted as clear sky pixels (see Figure 6a). Meanwhile, the SPO station shows substantial warm biases in winter for the MYD21 and the VNP21, which are consistent with the above findings, and it can be attributed to the warm bias of atmospheric reanalysis in the polar region, especially during winter.

Table 3. Assessment accuracies of the four IST products for eight stations in summer (DJF) and in winter (JJA).

IST Products		AWS5		AWS9		AWS11		AWS13		AWS16		Panda400		DOM		SPO	
		DJF	JJA	DJF	JJA	DJF	JJA	DJF	JJA	DJF	JJA	DJF	JJA	DJF	JJA	DJF	JJA
MYD11	N	339	149	401	305	161	105	542	412	224	91	382	138	438	622	514	830
	Bias	−1.80	−1.16	−2.45	−5.08	−1.74	−5.8	−1.26	−3.95	−2.36	−5.46	−1.97	−2.38	0.94	−3.72	−0.62	−2.78
	RMSE	2.79	1.91	3.39	6.46	2.82	7.28	2.42	5.14	4.12	5.95	2.74	3.4	1.71	4.84	1.36	5.01
MYD21	N	316	135	368	179	152	91	477	154	212	60	345	90	408	448	363	47
	Bias	−1.28	−0.07	−1.69	−2.85	−1.12	−4.68	−0.13	−1.88	−1.87	−4.28	−1.52	−1.08	−0.27	−1.89	1.13	3.36
	RMSE	2.53	1.54	2.66	3.76	2.34	6.24	2.11	2.95	3.83	4.85	2.53	2.33	1.26	3.42	1.6	4.74
VNP21	N	349	297	312	158	165	326	69	337	271	126	366	382	181	131	9	310
	Bias	−1.34	−0.78	−1.53	−0.93	−1.35	−3.4	−0.75	0.24	−0.99	−3.03	−1.38	−0.62	−0.2	0.11	0.03	3.11
	RMSE	2.45	2.13	2.47	4.56	2.62	4.95	1.53	3.53	3.98	4.55	2.17	1.93	1.25	3.3	0.61	4.95
VNP11	N									25		98	23				
	Bias									0.21		−1.31	−0.25				
	RMSE									1.68		1.72	1.9				

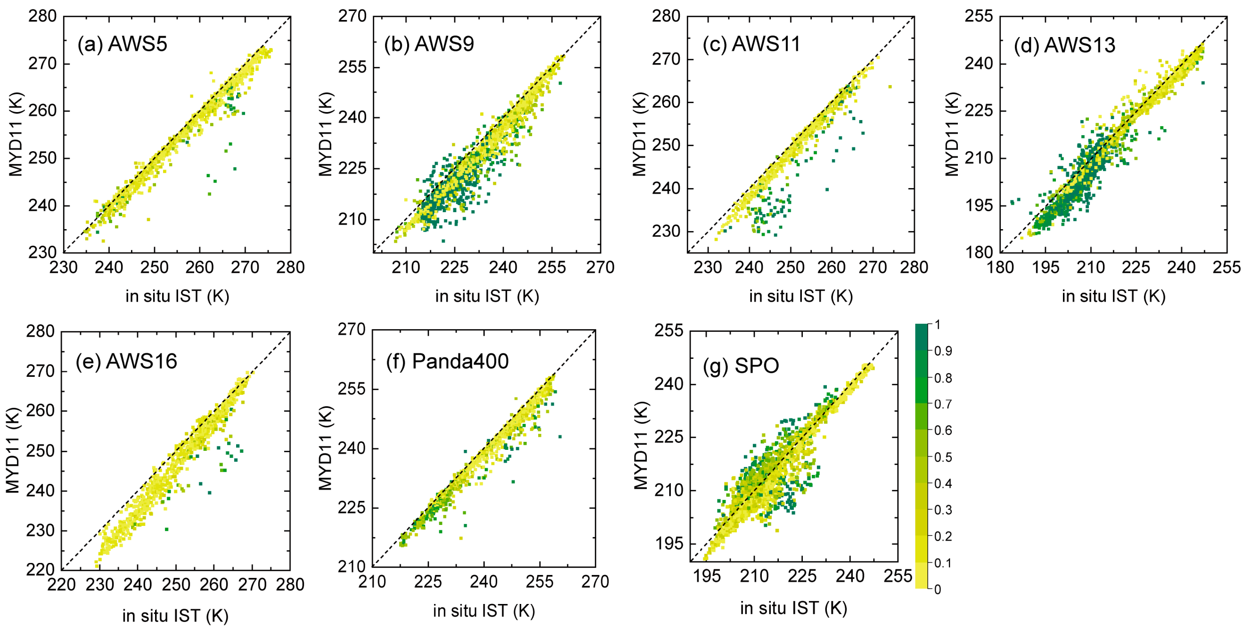

Figure 6. The color scatterplots of comparison results between the MYD11 and in situ IST. The color is closer to green, and the cloud index is closer to 1. The color is closer to yellow, and the cloud index is closer to 0.

3.2. Accuracy Comparison After Using the Cloud Index

To evaluate the impact of cloud misidentification on the accuracy of the MODIS and VIIRS IST products, the cloud index based on station data was used to distinguish IST pixels that are cloud-contaminated but incorrectly classified as clear sky in the satellite cloud mask product. Figure 6 exhibits the color scatterplot of the comparison results between the MYD11 and in situ IST data, where color represents the cloud index of all matched pixels identified as clear sky with the satellite cloud mask. When the color is closer to green (the closer n is to 1), it means that the point may be the cloud-contaminated pixels. Notably, many points of the MYD11 on the AWS5 station are close to a green color at higher temperatures, which may be the cloud contamination pixels, and further lead to a greater cold bias in summer than that in winter (Section 3.1). Moreover, the MYD11 in AWS9, AWS13, and SPO exhibit many green points, which are concentrated in the low-temperature range, and these points may be the cloud contamination pixels. Meanwhile, AWS9 may also be affected by rime, as the relative humidity was not used to remove the record affected by rime accumulation. Color scatterplots for the MYD21 and the VNP21 are not presented due to their similar spatial distribution, and this is also the case with the MYD11.

An n less than 0.2 is treated as a clear sky for further comparison, while the remote sensing IST values before applying the cloud index are considered as all skies (as described in Section 3.1). Therefore, by comparing the differences in validation accuracy between clear sky and all sky, the impact of an incorrect cloud mask on the validation results can be demonstrated. Figure 7 is the comparison results between all sky and clear sky, and Figure 7a–d are for the MYD11, MYD21, VNP21, and VNP11, respectively. The overall accuracies for clear sky are better than that in all sky for the four products, where the cold biases and RMSEs are smaller for clear sky. Specifically, for the MYD11 (Figure 7a), the total RMSEs decreased from 0.48K to 2.1 K, the cold biases decreased by 0.3–1.26 K for different stations after using the cloud index, and the validation accuracy at the SPO station shows a larger cold bias after applying the cloud index. The primary reason is because there were some low-altitude thin clouds over the interior plateau with temperatures higher than the snow surface, and these thin clouds do not alter the inversion temperature structure. Similarly, for the MYD21 (VNP21) IST, the total RMSEs decrease by 0.46–1.94 K (0.46–3.51 K), and the cold biases decrease by 0.18–0.91 K (0.04–1.36 K). However, for the SPO station, both the MYD21 and the VNP21 have reduced warm bias, as explained in the MYD11 for the SPO station. In conclusion, after removing the misidentified cloud pixels in the MODIS cloud mask, the validation accuracies were prominently improved.

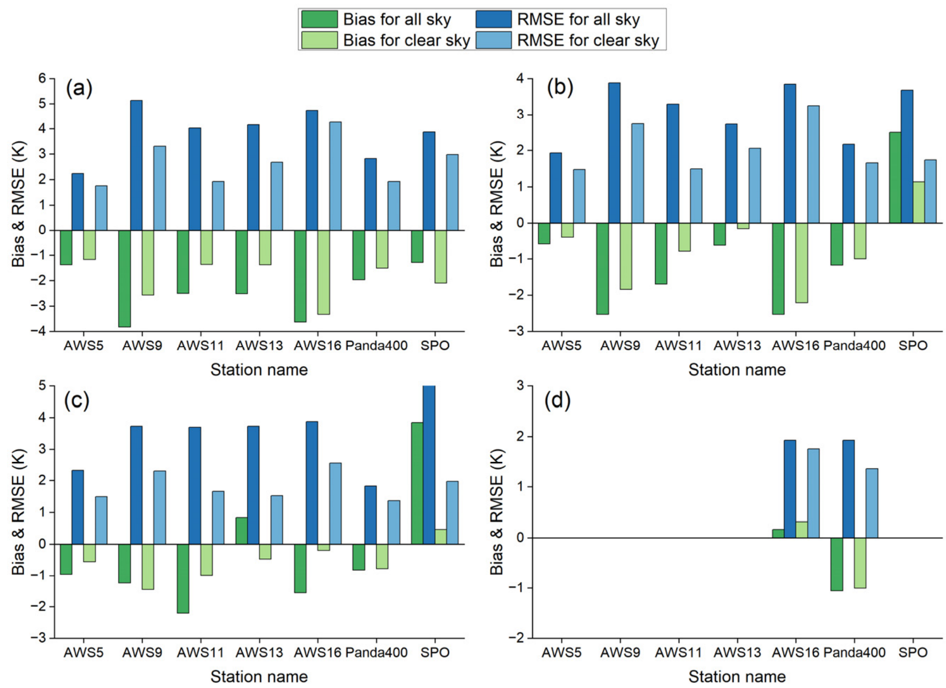

Figure 7. The validation accuracies between all sky and clear sky for the four products. (**a**–**d**) are for the MYD11, MYD21, VNP21, and VNP11, respectively.

4. Discussion

4.1. Uncertainty of In Situ IST

Generally, the accurate calculation of the in situ IST depends on the magnitude of the uncertainties in the broadband radiation and the broadband emissivity of snow. For the broadband radiometer, the uncertainty measured in laboratory was about 10%. However, some comparative experiments in the polar region and glaciers have shown that a radiometer generally has less uncertainty. For example, the maximum daily uncertainty assessed for the CNR1 radiometer was about 5% in Queen Maud Land of the Antarctic [17], the Eppley PIR radiometer used at the south pole (SPO) had an uncertainty of about 4 W/m^2 [66], and the uncertainty of downward broadband radiation for CNR1 over an Alpine glacier was less than 2 W/m^2, resulting in the uncertainty of the in situ IST being less than 0.5 K [67]. Meanwhile, the broadband emissivity of snow varies with the size and the density of snow particles. In previous studies, the broadband emissivity of snow was set as 0.970 [68], 0.985 [3,43], and 0.990 [69], and different broadband emissivity values will lead to differences in the calculation of the in situ IST, subsequently affecting the final assessment accuracy. Here, we quantify how much variation in the in situ IST affects the assessment accuracy for the different emissivity values of snow. Figure 8 demonstrates that the bias and RMSE will improve with increasing broadband emissivity, with approximately every 0.01 increase in the broadband emissivity value leading to an improvement in bias of 0.2 K. From the above analyses, the total validation accuracy cannot be explained by the uncertainty of broadband radiation and snow emissivity. Meanwhile, a recent study indicated that the atmospheric radiation between the radiometer and surface is neglected, which may lead to an overestimation of in situ ISTs at night in the mid-latitude region [49]. Therefore, we think that ignoring the near-surface atmospheric radiation between the broadband radiometer and snow surface could be a reason for the cold bias of IST validation in the polar region, and more studies about the near-surface atmospheric radiation need to be implemented in the future.

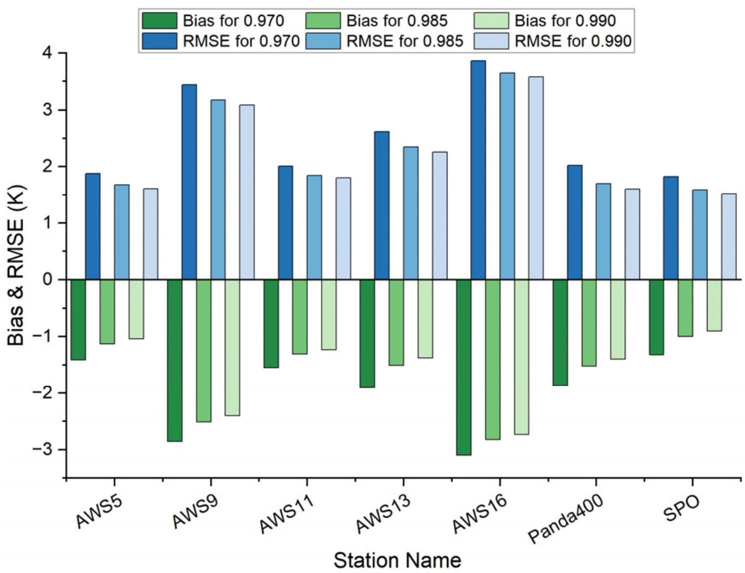

Figure 8. The assessment accuracies of the remote sensing IST with the in situ IST for different values of broadband emissivity. Green represents bias, and the blue color is the RMSE.

4.2. Uncertainty of Clouds

Clouds strongly affect the application of remote sensing IST products in the polar region. On the one hand, the widespread presence of clouds result in a low proportion of IST pixels, especially in coastal areas [70]. On the other hand, it is difficult to distinguish between the cloud and the snow surface due to their similar spectra, thus misidentifying cloudy pixels as clear sky pixels for IST production [40,43]. Meanwhile, cloud height, cloud phase, cloud thickness, and cloud cover are different across the Antarctic ice sheet, which lead to colossal differences in the accuracy of cloud identification for different stations. Here, the numbers of each cloud index value for different stations are counted (except DOM), as shown in Figure 9. The distribution ratios of the cloud index for all stations vary greatly, indicating the obvious differences in cloud proportions across different regions.

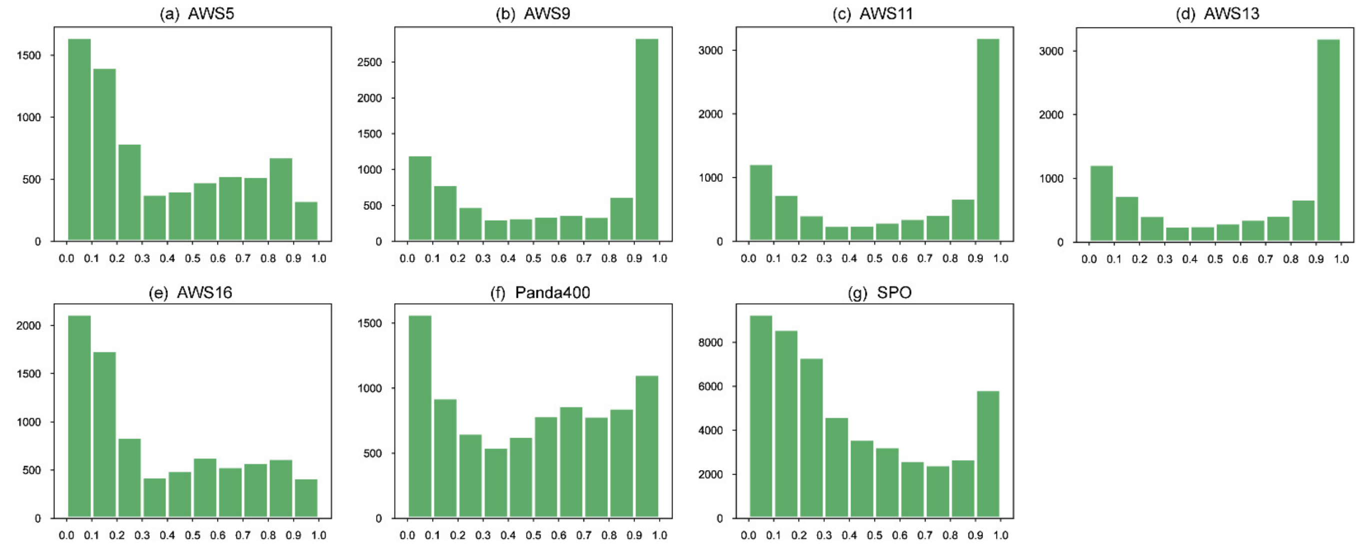

Figure 9. The statistics of the numbers of each cloud index value for different stations.

Meanwhile, the visible light bands of satellites are unavailable during polar night, which leads to obvious differences in the cloud identification accuracy between winter and summer in the polar region [71]. The number of different sky conditions, including clear sky ($n < 0.2$), cloudy ($n > 0.8$), and mixed ($0.2 < n < 0.8$), are counted, as shown in Figure 10, where green represents the statistical results in summer, and blue is for winter. Figure 10a,b show the statistical results for the MYD11, Figure 10c,d for the MYD21, and Figure 10e,f for the VNP21. Although the proportions of different sky conditions vary across different stations and different remote sensing IST products, a consistent pattern can be observed, where the proportion of cloudy or mixed sky conditions in winter is prominently higher than those in summer. This indicates that the rate of cloud misidentification is lower during the polar day compared with the results in the polar night. Therefore, extra caution should be exercised when using remote sensing IST products under polar night.

Although the cloud index ($n < 0.2$) is regarded as clear sky in this study, the n less than 0.2 cannot completely filter out the cloudy sky because n is essentially the characteristic for cloud optical thickness [57]. On one hand, when the cloud pattern is higher and thinner, the downward broadband radiation of clouds is very small, resulting in an n below 0.2, but there is, in fact, a cloudy sky. On the other hand, since the cloud index represents the vertical distribution of clouds and considering the change in the satellite observation azimuth angle, the absence of a cloud in the vertical direction does not mean that there is no cloud in the satellite observation angle. Even so, using the cloud index can effectively remove the incorrect cloud mask pixels to improve the validation accuracy of the IST in the polar region.

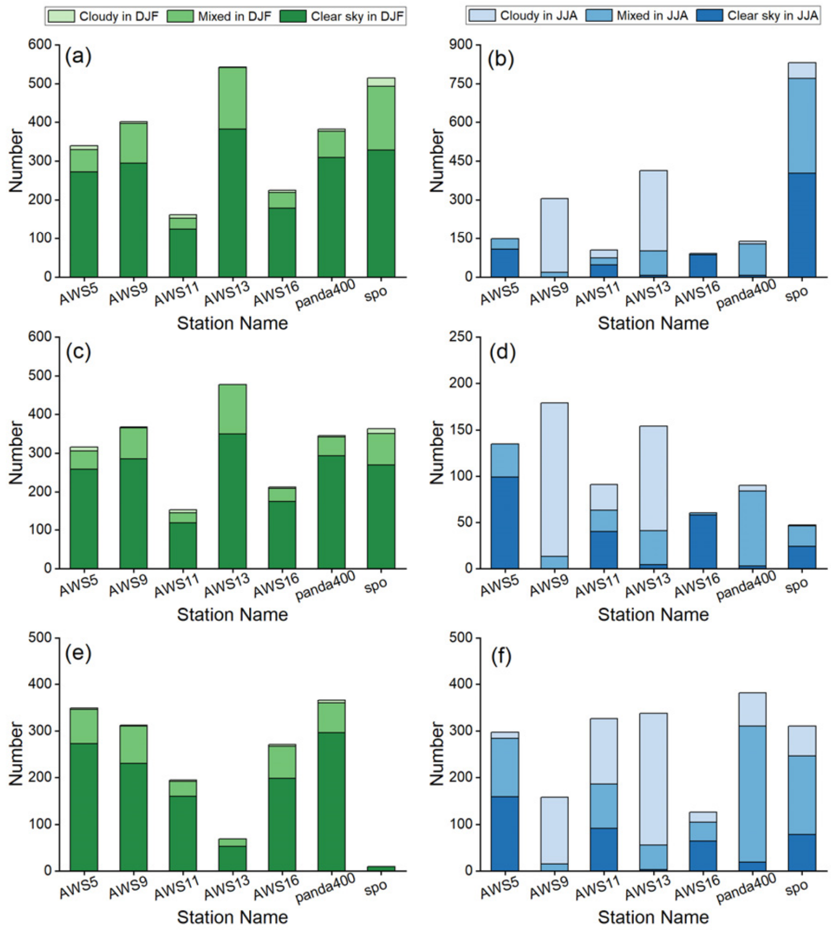

Figure 10. The number of different sky conditions (cloudy, mixed, and clear sky) in summer and winter for three IST products. Green color is the result in summer and blue color for winter; (**a**,**b**) are for MYD11; (**c**,**d**) are for MYD21; (**e**,**f**) are for VNP21.

4.3. Differences Between SW-Based IST and TES-Based IST

To compare the differences in validation accuracy between the TES-based IST and SW-based IST on the ice or snow surface, the values of n less than 0.2 are selected to ensure that cloud containment pixels are excluded in this section, and the pixels for two products (for the MODIS sensor) are at the same time extracted for comparison. Figure 11 shows the comparison accuracies of the TES-based IST and SW-based IST. The uncertainty and cold bias of the TES-based IST is smaller than the SW-based IST in Figure 11 (SPO excluded), which shows that the TES-based IST can improve the cold bias of the SW-based IST, which is consistent with the results from previous studies in non-glacial regions [34]. In addition, the characteristics of dynamic retrieval of the IST and emissivity for the TES-based method can make up for the shortcoming of the fixed emissivity values based on the SW-based method, especially for more widespread melting regions of the Antarctic ice sheet in summer. Although the accuracy of the TES-based algorithm may be better than the SW-based algorithm, there is a certain warm bias found in the Antarctic inland plateau, which may be related to the warm bias of the reanalysis data used for the TES-based algorithm, as mentioned above. Hence, using other reanalysis data to improve the retravel accuracy of the TES-based algorithm or other methods needs to be explored in the future.

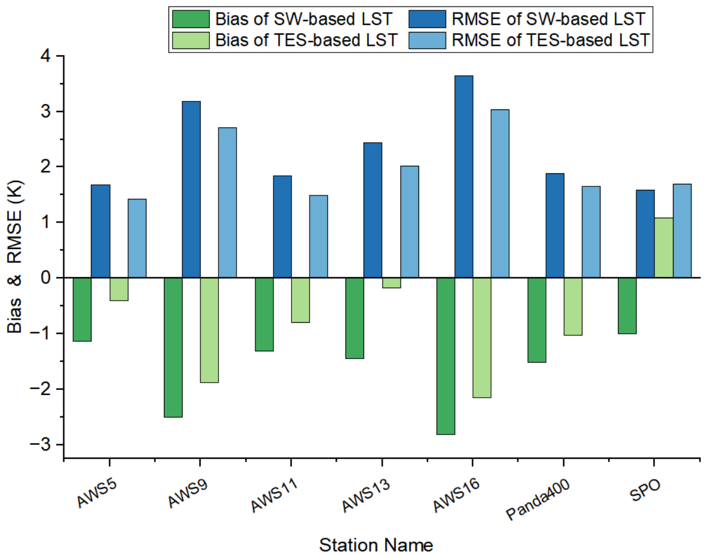

Figure 11. Comparison accuracies between TES-based IST and SW-based IST.

4.4. Assessment Accuracy Differences of IST Under Different Temperature Gradients

To explore whether the assessment accuracies of the remote sensing IST vary with temperature gradients, here we divide the IST gradients by temperature intervals of 10 K. Considering the number of extreme low temperatures and the boundary of the highest IST, the six IST gradients are divided, which are 190–220 K, 220–230 K, 230–240 K, 240–250 K, 250–260 K, and 260–275 K. Figure 12 shows the histogram of temperature differences (ΔIST) between the in situ IST and remote sensing IST alongside the assessment accuracies. Figure 12a–f are the results of the SW-based IST, and Figure 12g–l are for the TES-based IST. For the bias and RMSE of different IST gradients, as the IST decreases, both biases and RMSEs will increase, whereas a higher IST is associated with a smaller bias and RMSE. As described in Section 4.1, this gradual cold bias may result from the near-surface atmospheric radiation not being accounted for in the calculation of the in situ IST. Meanwhile, temperature inversion plays a vital role in the near-surface atmospheric radiation, which further leads to a larger cold bias in the IST validation under colder conditions.

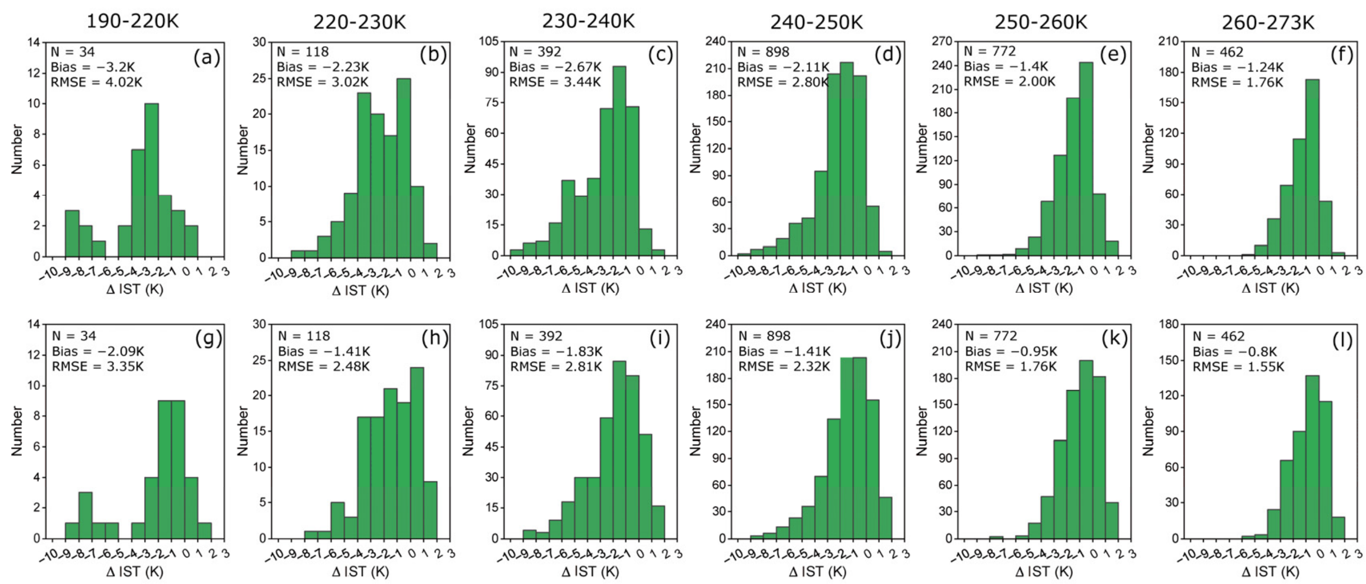

Figure 12. The histogram of the temperature differences (ΔIST) between the in situ IST and remote sensing IST and the assessment accuracy: (**a**–**f**) are for the SW-based IST and (**g**–**l**) are for the TES-based IST.

4.5. Others

As previously mentioned, the remote sensing IST validation, with the in situ IST derived from broadband radiation, has difficulty meeting the 1 K accuracy, which also exists in the mid-latitude regions [48,49,62]. However, due to the limited availability of narrow infrared radiation data in the Antarctic, efforts should focus on deploying narrow infrared radiation instruments in the Antarctic ice sheet to accurately calculate in situ IST and further to validate remote sensing IST in the future. Furthermore, this study evaluated the VNP11 product by using only two stations, and due to the scarcity of station data and the temporal availability of the VNP11, future research should focus on the evaluation of the VNP11 product using more stations. Finally, although this study assessed and analyzed the uncertainties associated with both the stations and satellites, further research is needed to fully address the sources of cold bias in IST validation. Especially, how to correct the broadband radiation IST by considering the near-surface atmospheric radiation needs to be further explored and solved.

5. Conclusions

This study utilized eight broadband radiation ISTs to assess the latest released MODIS and VIIRS swath level 2 IST products (SW-based and TES-based) and analyzed the source of uncertainty in the validation process, which aims to understand the uncertainties in the remote sensing IST and challenges in the IST validation process.

The results show substantial errors when using the in situ IST to evaluate the remote sensing IST, where the pixels are misidentified as clear sky in satellite cloud mask products. These errors are primarily due to the spectral similarities between cloud and snow, which make it difficult to distinguish cloud and snow from remote sensing images. Furthermore, the types and the quantities of clouds vary substantially for different climatic zones in the Antarctic ice sheet, leading to the rates of cloud misidentification varying with different stations. This, in turn, contributes to discrepancies in the IST validation results across different stations. A cloud index (n), based on the relationship between air temperature and downward broadband radiation at the station scale, was used to remove pixels marked as clear sky but clouds pixels in the cloud mask products. After applying the cloud index, the overall validation accuracy concentrated around 2–3 K, with the maximum RMSE reduced by 3.51 K and the bias reduced by 1.26 K.

However, even after excluding incorrect cloud pixels using the cloud index, the validation results still exhibited a progressive cold bias, with the bias increasing as the temperature decreased. The analysis suggests that this might be the calculation errors of the in situ IST, which can be attributed to the atmospheric radiation between the radiometer and the snow surface, which was not considered in previous studies. Finally, the analysis reveals that the proportion of misidentified cloud pixels is higher during the winter compared to that in the summer, suggesting that caution is necessary when using IST products directly. This study also highlights the importance of deploying infrared radiometers in the future to minimize the influence of near-surface atmospheric radiation on the broadband radiation IST, enabling more accurate assessments of ice and snow surface temperatures in the polar region.

Author Contributions: Conceptualization, C.S. and Y.W.; methodology, C.S.; software, C.S.; data curation, C.S., P.C.J.P.S. and C.H.R.; writing—original draft preparation, C.S.; writing—review and editing, N.W.; visualization, C.S. and Q.Z.; supervision, N.W. All authors have read and agreed to the published version of the manuscript.

Funding: This work was funded by the National Natural Science Foundation of China (Grant No. 41971088).

Data Availability Statement: The data will be made available on request.

Acknowledgments: The authors thank BSRN, IMAU, and Panda AWS network for providing in situ data.

Conflicts of Interest: The authors declare no conflicts of interest.

References

1. Li, Z.-L.; Tang, B.-H.; Wu, H.; Ren, H.; Yan, G.; Wan, Z.; Trigo, I.F.; Sobrino, J.A. Satellite-derived land surface temperature: Current status and perspectives. *Remote Sens. Environ.* **2013**, *131*, 14–37. [CrossRef]
2. Adolph, A.C.; Albert, M.R.; Hall, D.K. Near-surface temperature inversion during summer at Summit, Greenland, and its relation to MODIS-derived surface temperatures. *Cryosphere* **2018**, *12*, 907–920. [CrossRef]
3. Yu, X.; Wang, T.; Ding, M.; Wang, Y.; Sun, W.; Zhang, Q.; Huai, B. Assessment of MODIS Surface Temperature Products of Greenland Ice Sheet Using In-Situ Measurements. *Land* **2022**, *11*, 593. [CrossRef]
4. Fréville, H.; Brun, E.; Picard, G.; Tatarinova, N.; Arnaud, L.; Lanconelli, C.; Reijmer, C.; Van den Broeke, M. Using MODIS land surface temperatures and the Crocus snow model to understand the warm bias of ERA-Interim reanalyses at the surface in Antarctica. *Cryosphere* **2014**, *8*, 1361–1373. [CrossRef]
5. Hall, D.K.; Box, J.E.; Casey, K.A.; Hook, S.J.; Shuman, C.A.; Steffen, K. Comparison of satellite-derived and in-situ observations of ice and snow surface temperatures over Greenland. *Remote Sens. Environ.* **2008**, *112*, 3739–3749. [CrossRef]
6. Pörtner, H.-O.; Roberts, D.C.; Masson-Delmotte, V.; Zhai, P.; Tignor, M.; Poloczanska, E.; Weyer, N. The ocean and cryosphere in a changing climate. *IPCC Spec. Rep. Ocean Cryosphere Chang. Clim.* **2019**, *1155*, 10–17.
7. Jansen, E.; Christensen, J.H.; Dokken, T.; Nisancioglu, K.H.; Vinther, B.M.; Capron, E.; Guo, C.; Jensen, M.F.; Langen, P.L.; Pedersen, R.A. Past perspectives on the present era of abrupt Arctic climate change. *Nat. Clim. Change* **2020**, *10*, 714–721. [CrossRef]
8. Rantanen, M.; Karpechko, A.Y.; Lipponen, A.; Nordling, K.; Hyvärinen, O.; Ruosteenoja, K.; Vihma, T.; Laaksonen, A. The Arctic has warmed nearly four times faster than the globe since 1979. *Commun. Earth Environ.* **2022**, *3*, 168. [CrossRef]
9. Jun, S.-Y.; Kim, J.-H.; Choi, J.; Kim, S.-J.; Kim, B.-M.; An, S.-I. The internal origin of the west-east asymmetry of Antarctic climate change. *Sci. Adv.* **2020**, *6*, eaaz1490. [CrossRef]
10. Sato, K.; Simmonds, I. Antarctic skin temperature warming related to enhanced downward longwave radiation associated with increased atmospheric advection of moisture and temperature. *Environ. Res. Lett.* **2021**, *16*, 064059. [CrossRef]
11. Steig, E.J.; Schneider, D.P.; Rutherford, S.D.; Mann, M.E.; Comiso, J.C.; Shindell, D.T. Warming of the Antarctic ice-sheet surface since the 1957 International Geophysical Year. *Nature* **2009**, *457*, 459–462. [CrossRef] [PubMed]
12. Turner, J.; Marshall, G.; Clem, K.; Colwell, S.; Phillips, T.; Lu, H. Antarctic temperature variability and change from station data. *Int. J. Climatol.* **2020**, *40*, 2986–3007. [CrossRef]
13. Comiso, J.C. Variability and trends in Antarctic surface temperatures from in situ and satellite infrared measurements. *J. Clim.* **2000**, *13*, 1674–1696. [CrossRef]
14. Comiso, J.C.; Gersten, R.A.; Stock, L.V.; Turner, J.; Perez, G.J.; Cho, K. Positive trend in the Antarctic sea ice cover and associated changes in surface temperature. *J. Clim.* **2017**, *30*, 2251–2267. [CrossRef]
15. Chapman, W.L.; Walsh, J.E. A synthesis of Antarctic temperatures. *J. Clim.* **2007**, *20*, 4096–4117. [CrossRef]
16. Turner, J.; Colwell, S.R.; Marshall, G.J.; Lachlan-Cope, T.A.; Carleton, A.M.; Jones, P.D.; Lagun, V.; Reid, P.A.; Iagovkina, S. Antarctic climate change during the last 50 years. *Int. J. Climatol.* **2005**, *25*, 279–294. [CrossRef]
17. van den Broeke, M.; van As, D.; Reijmer, C.; van de Wal, R. Assessing and improving the quality of unattended radiation observations in Antarctica. *J. Atmos. Ocean. Technol.* **2004**, *21*, 1417–1431. [CrossRef]
18. Tian, T.; Yang, S.; Høyer, J.L.; Nielsen-Englyst, P.; Singha, S. Cooler Arctic surface temperatures simulated by climate models are closer to satellite-based data than the ERA5 reanalysis. *Commun. Earth Environ.* **2024**, *5*, 111. [CrossRef]
19. Bromwich, D.H.; Ensign, A.; Wang, S.H.; Zou, X. Major artifacts in ERA5 2-m air temperature trends over Antarctica prior to and during the modern satellite era. *Geophys. Res. Lett.* **2024**, *51*, e2024GL111907. [CrossRef]
20. Li, J.; Zwally, H.J.; Comiso, J.C. Ice-sheet elevation changes caused by variations of the firn compaction rate induced by satellite-observed temperature variations (1982–2003). *Ann. Glaciol.* **2007**, *46*, 8–13. [CrossRef]
21. Wang, Y.; Wang, M.; Zhao, J. A comparison of MODIS LST retrievals with in situ observations from AWS over the Lambert Glacier Basin, East Antarctica. *Int. J. Geosci.* **2013**, *4*, 611–617. [CrossRef]
22. McClain, E.P.; Pichel, W.G.; Walton, C.C. Comparative performance of AVHRR-based multichannel sea surface temperatures. *J. Geophys. Res. Oceans* **1985**, *90*, 11587–11601. [CrossRef]
23. Wan, Z.; Zhang, Y.; Zhang, Q.; Li, Z.-L. Quality assessment and validation of the MODIS global land surface temperature. *Int. J. Remote Sens.* **2004**, *25*, 261–274. [CrossRef]

24. Guillevic, P.C.; Privette, J.L.; Coudert, B.; Palecki, M.A.; Demarty, J.; Ottlé, C.; Augustine, J.A. Land Surface Temperature product validation using NOAA's surface climate observation networks—Scaling methodology for the Visible Infrared Imager Radiometer Suite (VIIRS). *Remote Sens. Environ.* **2012**, *124*, 282–298. [CrossRef]
25. Ciappa, A.; Pietranera, L.; Budillon, G. Observations of the Terra Nova Bay (Antarctica) polynya by MODIS ice surface temperature imagery from 2005 to 2010. *Remote Sens. Environ.* **2012**, *119*, 158–172. [CrossRef]
26. Kerr, Y.H.; Lagouarde, J.P.; Imbernon, J. Accurate land surface temperature retrieval from AVHRR data with use of an improved split window algorithm. *Remote Sens. Environ.* **1992**, *41*, 197–209. [CrossRef]
27. Wang, X.; Key, J.R. Arctic surface, cloud, and radiation properties based on the AVHRR Polar Pathfinder dataset. Part I: Spatial and temporal characteristics. *J. Clim.* **2005**, *18*, 2558–2574. [CrossRef]
28. Hall, D.K.; Comiso, J.C.; DiGirolamo, N.E.; Shuman, C.A.; Box, J.E.; Koenig, L.S. Variability in the surface temperature and melt extent of the Greenland ice sheet from MODIS. *Geophys. Res. Lett.* **2013**, *40*, 2114–2120. [CrossRef]
29. Key, J.; Wang, X.; Liu, Y.; Dworak, R.; Letterly, A. The AVHRR polar pathfinder climate data records. *Remote Sens.* **2016**, *8*, 167. [CrossRef]
30. Comiso, J.C. Warming trends in the Arctic from clear sky satellite observations. *J. Clim.* **2003**, *16*, 3498–3510. [CrossRef]
31. Justice, C.; Townshend, J.; Vermote, E.; Masuoka, E.; Wolfe, R.; Saleous, N.; Roy, D.; Morisette, J. An overview of MODIS Land data processing and product status. *Remote Sens. Environ.* **2002**, *83*, 3–15. [CrossRef]
32. Xiong, X.; Butler, J.J. MODIS and VIIRS calibration history and future outlook. *Remote Sens.* **2020**, *12*, 2523. [CrossRef]
33. Liu, Y.; Yu, Y.; Yu, P.; Wang, H.; Rao, Y. Enterprise LST algorithm development and its evaluation with NOAA 20 data. *Remote Sens.* **2019**, *11*, 2003. [CrossRef]
34. Li, H.; Li, R.; Yang, Y.; Cao, B.; Bian, Z.; Hu, T.; Du, Y.; Sun, L.; Liu, Q. Temperature-based and radiance-based validation of the collection 6 MYD11 and MYD21 land surface temperature products over barren surfaces in northwestern China. *IEEE Trans. Geosci. Remote Sens.* **2020**, *59*, 1794–1807. [CrossRef]
35. Yang, J.; Zhou, J.; Göttsche, F.-M.; Long, Z.; Ma, J.; Luo, R. Investigation and validation of algorithms for estimating land surface temperature from Sentinel-3 SLSTR data. *Int. J. Appl. Earth Obs. Geoinf.* **2020**, *91*, 102136. [CrossRef]
36. Scambos, T.A.; Haran, T.M.; Massom, R. Validation of AVHRR and MODIS ice surface temperature products using in situ radiometers. *Ann. Glaciol.* **2006**, *44*, 345–351. [CrossRef]
37. Liu, Y.; Key, J.; Tschudi, M.; Dworak, R.; Mahoney, R.; Baldwin, D. Validation of the Suomi NPP VIIRS ice surface temperature environmental data record. *Remote Sens.* **2015**, *7*, 17258–17271. [CrossRef]
38. Shuman, C.A.; Hall, D.K.; DiGirolamo, N.E.; Mefford, T.K.; Schnaubelt, M.J. Comparison of near-surface air temperatures and MODIS ice-surface temperatures at Summit, Greenland (2008–2013). *J. Appl. Meteorol. Climatol.* **2014**, *53*, 2171–2180. [CrossRef]
39. Hall, D.K.; Key, J.R.; Casey, K.A.; Riggs, G.A.; Cavalieri, D.J. Sea ice surface temperature product from MODIS. *IEEE Trans. Geosci. Remote Sens.* **2004**, *42*, 1076–1087. [CrossRef]
40. Westermann, S.; Langer, M.; Boike, J. Systematic bias of average winter-time land surface temperatures inferred from MODIS at a site on Svalbard, Norway. *Remote Sens. Environ.* **2012**, *118*, 162–167. [CrossRef]
41. Dybkjær, G.; Tonboe, R.; Høyer, J. Arctic surface temperatures from Metop AVHRR compared to in situ ocean and land data. *Ocean Sci.* **2012**, *8*, 959–970. [CrossRef]
42. Hachem, S.; Duguay, C.; Allard, M. Comparison of MODIS-derived land surface temperatures with ground surface and air temperature measurements in continuous permafrost terrain. *Cryosphere* **2012**, *6*, 51–69. [CrossRef]
43. Østby, T.I.; Schuler, T.V.; Westermann, S. Severe cloud contamination of MODIS Land Surface Temperatures over an Arctic ice cap, Svalbard. *Remote Sens. Environ.* **2014**, *142*, 95–102. [CrossRef]
44. Fan, P.; Pang, X.; Zhao, X.; Shokr, M.; Lei, R.; Qu, M.; Ji, Q.; Ding, M. Sea ice surface temperature retrieval from Landsat 8/TIRS: Evaluation of five methods against in situ temperature records and MODIS IST in Arctic region. *Remote Sens. Environ.* **2020**, *248*, 111975. [CrossRef]
45. Zikan, K.H.; Adolph, A.C.; Brown, W.P.; Fausto, R.S. Comparison of MODIS surface temperatures to in situ measurements on the Greenland Ice Sheet from 2014 to 2017. *J. Glaciol.* **2023**, *69*, 129–140. [CrossRef]
46. Scambos, T.; Campbell, G.; Pope, A.; Haran, T.; Muto, A.; Lazzara, M.; Reijmer, C.; Van den Broeke, M. Ultralow surface temperatures in East Antarctica from satellite thermal infrared mapping: The coldest places on Earth. *Geophys. Res. Lett.* **2018**, *45*, 6124–6133. [CrossRef]
47. Liu, T.; Wang, Z.; Huang, X.; Cao, L.; Niu, M.; Tian, Z. An effective Antarctic ice surface temperature retrieval method for MODIS. *Photogramm. Eng. Remote Sens.* **2015**, *81*, 861–872. [CrossRef]
48. Guillevic, P.; Göttsche, F.; Nickeson, J.; Hulley, G.; Ghent, D.; Yu, Y.; Trigo, I.; Hook, S.; Sobrino, J.A.; Remedios, J. *Land Surface Temperature Product Validation Best Practice Protocol Version 1.0-October, 2017*; NASA: Washington, DC, USA, 2017.
49. Ma, J.; Zhou, J.; Zhang, T.; Tang, W.; Wang, Y. A Comprehensive Validation Scheme for Satellite-derived Land Surface Temperature Dataset. *IEEE Trans. Geosci. Remote Sens.* **2024**, *62*, 5007812. [CrossRef]

50. Liu, T.; Li, Y.; Wang, Z.; Yuan, Q. A new Spatially and Temporally Continuous Antarctic Ice-sheet Surface Temperature Retrieval Method from Passive Microwave Swath Data. *IEEE J. Sel. Top. Appl. Earth Obs. Remote Sens.* **2024**, *17*, 10690–10702. [CrossRef]
51. Bromwich, D.H.; Nicolas, J.P.; Monaghan, A.J.; Lazzara, M.A.; Keller, L.M.; Weidner, G.A.; Wilson, A.B. Central West Antarctica among the most rapidly warming regions on Earth. *Nat. Geosci.* **2013**, *6*, 139–145. [CrossRef]
52. Gerace, A.; Kleynhans, T.; Eon, R.; Montanaro, M. Towards an operational, split window-derived surface temperature product for the thermal infrared sensors onboard Landsat 8 and 9. *Remote Sens.* **2020**, *12*, 224. [CrossRef]
53. Krishnan, P.; Meyers, T.P.; Hook, S.J.; Heuer, M.; Senn, D.; Dumas, E.J. Intercomparison of in situ sensors for ground-based land surface temperature measurements. *Sensors* **2020**, *20*, 5268. [CrossRef] [PubMed]
54. Smeets, P.C.; Kuipers Munneke, P.; Van As, D.; van den Broeke, M.R.; Boot, W.; Oerlemans, H.; Snellen, H.; Reijmer, C.H.; van de Wal, R.S. The K-transect in west Greenland: Automatic weather station data (1993–2016). *Arct. Antarct. Alp. Res.* **2018**, *50*, S100002. [CrossRef]
55. Driemel, A.; Augustine, J.; Behrens, K.; Colle, S.; Cox, C.; Cuevas-Agulló, E.; Denn, F.M.; Duprat, T.; Fukuda, M.; Grobe, H. Baseline Surface Radiation Network (BSRN): Structure and data description (1992–2017). *Earth Syst. Sci. Data* **2018**, *10*, 1491–1501. [CrossRef]
56. Ding, M.; Zou, X.; Sun, Q.; Yang, D.; Zhang, W.; Bian, L.; Lu, C.; Allison, I.; Heil, P.; Xiao, C. The PANDA automatic weather station network between the coast and Dome A, East Antarctica. *Earth Syst. Sci. Data* **2022**, *14*, 5019–5035. [CrossRef]
57. Van Den Broeke, M.; Reijmer, C.; Van As, D.; Boot, W. Daily cycle of the surface energy balance in Antarctica and the influence of clouds. *Int. J. Climatol. J. R. Meteorol. Soc.* **2006**, *26*, 1587–1605. [CrossRef]
58. Duan, S.-B.; Li, Z.-L.; Zhao, W.; Wu, P.; Huang, C.; Han, X.-J.; Gao, M.; Leng, P.; Shang, G. Validation of Landsat land surface temperature product in the conterminous United States using in situ measurements from SURFRAD, ARM, and NDBC sites. *Int. J. Digit. Earth* **2021**, *14*, 640–660. [CrossRef]
59. Fang, Z.; Wang, N.; Wu, Y.; Zhang, Y. Greenland-ice-sheet surface temperature and melt extent from 2000 to 2020 and implications for mass balance. *Remote Sens.* **2023**, *15*, 1149. [CrossRef]
60. Wan, Z. New refinements and validation of the collection-6 MODIS land-surface temperature/emissivity product. *Remote Sens. Environ.* **2014**, *140*, 36–45. [CrossRef]
61. Hulley, G.C.; Malakar, N.K.; Islam, T.; Freepartner, R.J. NASA's MODIS and VIIRS land surface temperature and emissivity products: A long-term and consistent earth system data record. *IEEE J. Sel. Top. Appl. Earth Obs. Remote Sens.* **2017**, *11*, 522–535. [CrossRef]
62. Islam, T.; Hulley, G.C.; Malakar, N.K.; Radocinski, R.G.; Guillevic, P.C.; Hook, S.J. A physics-based algorithm for the simultaneous retrieval of land surface temperature and emissivity from VIIRS thermal infrared data. *IEEE Trans. Geosci. Remote Sens.* **2016**, *55*, 563–576. [CrossRef]
63. Hulley, G.C.; Hook, S.J. Generating consistent land surface temperature and emissivity products between ASTER and MODIS data for earth science research. *IEEE Trans. Geosci. Remote Sens.* **2010**, *49*, 1304–1315. [CrossRef]
64. Giesen, R.; Van den Broeke, M.; Oerlemans, J.; Andreassen, L. Surface energy balance in the ablation zone of Midtdalsbreen, a glacier in southern Norway: Interannual variability and the effect of clouds. *J. Geophys. Res. Atmos.* **2008**, *113*, D21111. [CrossRef]
65. Hulley, G.; Malakar, N.; Hughes, T.; Islam, T.; Hook, S. *Moderate Resolution Imaging Spectroradiometer (MODIS) MOD21 Land Surface Temperature and Emissivity Algorithm Theoretical Basis Document*; National Aeronautics and Space Administration Jet Propulsion Laboratory, California Institute of Technology: Pasadena, CA, USA, 2016.
66. Hudson, S.R.; Brandt, R.E. A look at the surface-based temperature inversion on the Antarctic Plateau. *J. Clim.* **2005**, *18*, 1673–1696. [CrossRef]
67. Michel, D.; Philipona, R.; Ruckstuhl, C.; Vogt, R.; Vuilleumier, L. Performance and uncertainty of CNR1 net radiometers during a one-year field comparison. *J. Atmos. Ocean. Technol.* **2008**, *25*, 442–451. [CrossRef]
68. Shahi, S.; Abermann, J.; Heinrich, G.; Prinz, R.; Schöner, W. Regional variability and trends of temperature inversions in Greenland. *J. Clim.* **2020**, *33*, 9391–9407. [CrossRef]
69. Nielsen-Englyst, P.; Høyer, J.L.; Madsen, K.S.; Tonboe, R.; Dybkjær, G.; Alerskans, E. In situ observed relationships between snow and ice surface skin temperatures and 2 m air temperatures in the Arctic. *Cryosphere* **2019**, *13*, 1005–1024. [CrossRef]
70. Vüllers, J.; Achtert, P.; Brooks, I.M.; Tjernström, M.; Prytherch, J.; Burzik, A.; Neely III, R. Meteorological and cloud conditions during the Arctic Ocean 2018 expedition. *Atmos. Chem. Phys.* **2021**, *21*, 289–314. [CrossRef]
71. Frey, R.A.; Ackerman, S.A.; Holz, R.E.; Dutcher, S.; Griffith, Z. The continuity MODIS-VIIRS cloud mask. *Remote Sens.* **2020**, *12*, 3334. [CrossRef]